



**AIAA 99-1802**

**Computational Aeroacoustic Analysis  
of Slat Trailing-Edge Flow**

Bart A. Singer, David P. Lockard,  
Kenneth S. Brentner  
NASA Langley Research Center  
Hampton, VA 23681-2199

Mehdi R. Khorrami,  
Mert E. Berkman,  
Meelan Choudhari  
High Technology Corporation  
28 Research Drive  
Hampton, VA 23666

**5th AIAA/CEAS Aeroacoustics  
Conference**

10--12 May, 1999, Greater Seattle,  
Washington

## COMPUTATIONAL AEROACOUSTIC ANALYSIS OF SLAT TRAILING-EDGE FLOW

Bart A. Singer\*, David P. Lockard†  
 Kenneth S. Brentner‡  
 NASA Langley Research Center  
 Hampton, VA 23681-2199

Mehdi R. Khorrami§  
 Mert E. Berkman¶  
 Meelan Choudhari#  
 High Technology Corporation  
 28 Research Drive  
 Hampton, VA 23666

An acoustic analysis based on the Ffowcs Williams and Hawkins equation was performed for a high-lift system. As input, the acoustic analysis used unsteady flow data obtained from a highly resolved, time-dependent, Reynolds-averaged Navier-Stokes calculation. The analysis strongly suggests that vortex shedding from the trailing edge of the slat results in a high-amplitude, high-frequency acoustic signal, similar to that which was observed in a corresponding experimental study of the high-lift system.

### Introduction

Airframe-generated noise is an important component of the total noise radiated from commercial aircraft, especially during the approach portion of the flight path when the engines are run at reduced power. Recent studies by Davy and Remy<sup>1</sup> on a scale model Airbus aircraft indicate that the high-lift devices and landing gear are the main sources of airframe noise when the aircraft is configured for approach. Earlier tests on a model of a DC-10 also identified the high-lift system as an important airframe noise source.<sup>2</sup> Dobrzynski, Nagakura, Gehlhar, and Buschbaum<sup>3</sup> performed full-scale ex-

perimental studies in an open-jet wind tunnel of a portion of a wing equipped with a high-lift system. They found that both the leading-edge slat and the side edge of the trailing flap contributed significantly to the airframe noise.

An extensive experimental and computational effort to study the various mechanisms associated with airframe-generated noise is currently underway at NASA Langley Research Center.<sup>4</sup> Considerable progress has already been made in understanding various aspects of the noise-generation process on the flap side edge.<sup>5-11</sup> More recently, attention has focussed on noise generated in the vicinity of the leading-edge slat.

A cooperative test involving NASA's High-Lift Program Element and NASA's Airframe Noise Team was conducted in NASA Langley Research Center's Low-Turbulence Pressure Tunnel (LTPT). Variation of the pressure in the tunnel allows the Reynolds number to be changed at constant Mach number. In these tests, the Reynolds number based on the cruise-wing chord varied from 3.6 to 19 million. No qualitative changes were observed in the data for Reynolds numbers above 7.2 million. The model tested in the tunnel is known as the Energy Efficient Transport (EET) model.<sup>12</sup> The EET model tested includes a full-span leading-edge slat and a part-span trailing flap. To obtain acoustic data, members of Boeing Commercial Airplane Company designed and built a microphone array that was installed in the ceiling of the wind tunnel. The microphone array and the subsequent data processing followed techniques developed earlier at Boeing.<sup>13</sup> These techniques have previously been used successfully to determine the noise radiated from localized sources, even in hard-walled, non-anechoic wind

\*Research Scientist, Aerodynamic and Acoustic Methods Branch.

†Research Scientist, Aerodynamic and Acoustic Methods Branch, Member AIAA.

‡Senior Research Engineer, Aerodynamic and Acoustic Methods Branch, Senior Member AIAA.

§Senior Scientist, Senior Member AIAA.

¶Senior Research Scientist, Senior Member AIAA.

#Research Scientist, Member AIAA.

Copyright ©1999 by the American Institute of Aeronautics and Astronautics, Inc. No copyright is asserted in the United States under Title 17, U.S. Code. The U.S. Government has a royalty-free license to exercise all rights under the copyright claimed herein for government purposes. All other rights are reserved by the copyright owner.

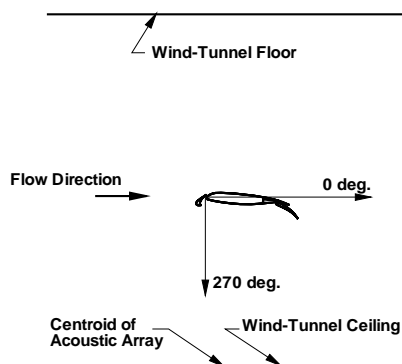


Figure 1. Schematic of model in wind tunnel. Flow from left to right. Acoustic directivity angles 0 and 270 deg. are indicated. View is rotated relative to experimental setup.

tunnels like the LTPT. To measure noise radiating groundward in normal flight, the EET model was mounted upside-down in the tunnel so that the pressure surface faced the array in the wind-tunnel ceiling. However, to reduce confusion, all references to directions in this paper will conform to the schematic of the experimental setup shown in Fig. 1. The view in Fig. 1 has been rotated from the physical orientation to one that is more intuitive. An enormous amount of data was collected and continues to be analyzed.

Figure 2 illustrates one unexpected and until recently, perplexing feature of the experimental data. For the case in which the slat deflection,  $\delta_s$ , is 30 degrees, a very large amplitude peak is observed in the acoustic spectrum in the vicinity of 50 kHz. This peak rises almost 20 dB above the signal observed for the case in which the slat is deflected 20 degrees. During the course of the experiment, efforts to eliminate the high-frequency peak by altering the overhang of the slat were largely unsuccessful. Only for cases in which the overhang became unrealistically large was a significant change in the high-frequency acoustic peak observed. Increasing the configuration's angle-of-attack from 10 to 15 degrees, reduced the amplitude of the high-frequency peak by approximately 10 dB. For some time, no consistent explanation of the observed phenomena was available. The focus of this paper and a companion paper<sup>14</sup> is to explain the observed large-amplitude, high-frequency peak in the experimentally obtained acoustic spec-

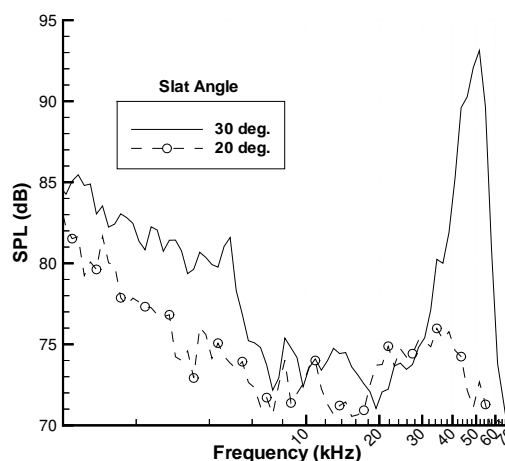


Figure 2. Acoustic spectrum based upon 1/12th octave bins with array focussed on slat region. Configuration angle of attack is 10 deg., Reynolds number is 7.2 million, Mach number is 0.2.

trum.

Khorrarni et al<sup>14</sup> provides details of unsteady, two-dimensional (2D), Reynolds-averaged Navier-Stokes (RANS) calculations designed to mimic the experimental conditions. In particular, the RANS computation was specially designed to properly incorporate and resolve the small, but finite trailing-edge thickness of the slat. Extremely small grid cells were used in the vicinity of the slat trailing edge and the time step was chosen to ensure more than 120 time steps per period of a 50 kHz signal. Initially calculations were performed with a slat trailing edge thickness  $h$  of approximately 0.07 percent of the cruise-wing chordlength  $C$ , which was an estimate of the actual slat trailing-edge thickness. Slat deflections of both 30 and 20 degrees were simulated. These calculations clearly show vortex shedding from the slat trailing edge for the case with a 30 degree slat deflection. Figure 3 shows a snapshot of the pressure fluctuations produced in the flow field. For physical reasons that are not yet clearly understood, the vortex shedding virtually disappears for the case of a 20 degree slat deflection. Acoustic analyses of the first set of data suggested that the initial grid distribution was insufficient to completely resolve the complex acoustic field in the cove and other regions in the vicinity of the slat. Later calculations with an enhanced grid were performed for a 30 degree slat deflection with  $h/C \approx 0.0009$ . The slat thickness was adjusted to more accurately represent the measured slat thickness on the model. In all cases,

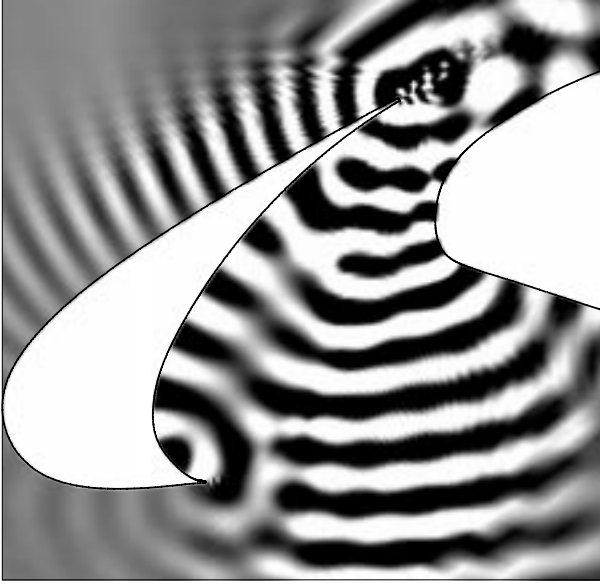


Figure 3. Instantaneous fluctuation pressure, in vicinity of leading-edge slat, from CFD calculation. Slat deflection is 30 deg. Wiggles at edges of dark and light bands are contouring artifacts.

the high cost of the calculations limited the duration of the temporal sample that was obtained. Here we discuss the use of that limited sample of unsteady computational data to perform acoustic analyses of the generated noise.

### Acoustic Procedure

Previously Singer et al<sup>15</sup> explored the use of unsteady computational data in acoustic-propagation codes based on the Ffowcs Williams and Hawkins<sup>16</sup> (hereafter referred to as FW-H) equation. Such codes compute the acoustic signal at a distant observer position by integrating the FW-H equation. Following Brentner and Farassat,<sup>17</sup> the FW-H equation may be written in differential form as

$$\begin{aligned} \square^2 p'(\mathbf{x}, t) &= \frac{\partial^2}{\partial x_i \partial x_j} [T_{ij} H(f)] \\ &- \frac{\partial}{\partial x_i} [L_i \delta(f)] + \frac{\partial}{\partial t} [(\rho_0 U_n) \delta(f)] \quad (1) \end{aligned}$$

where:  $\square^2 \equiv \frac{1}{c^2} \frac{\partial^2}{\partial t^2} - \nabla^2$  is the wave operator,  $c$  is the ambient speed of sound,  $t$  is observer time,  $p'$  is the acoustic pressure,  $\rho'$  is the perturbation density,  $\rho_0$  is the free-stream density,  $f = 0$  describes the integration surface,  $\delta(f)$  is the Dirac delta function, and  $H(f)$  is the Heaviside function. The quantities

$U_i$  and  $L_i$  are defined as

$$U_i = \left(1 - \frac{\rho}{\rho_0}\right) v_i + \frac{\rho u_i}{\rho_0} \quad (2)$$

and

$$L_i = P_{ij} \hat{n}_j + \rho u_i (u_n - v_n) \quad (3)$$

respectively. In the above equations,  $\rho$  is the total density,  $\rho u_i$ , is the momentum in the  $i$  direction,  $v_i$  is the velocity of the integration surface  $f = 0$ , and  $P_{ij}$  is the compressive stress tensor. For an inviscid fluid,  $P_{ij} = p' \delta_{ij}$  where  $\delta_{ij}$  is the Kronecker delta. The subscript  $n$  indicates the projection of a vector quantity in the surface-normal direction. To obtain a solution to Eq. (1), the first term on the right-hand-side must be integrated over the volume outside the integration surface  $f = 0$  wherever the Lighthill stress tensor  $T_{ij}$  is nonzero in this region. In the work reported here, this term is neglected. However the main effects of nonzero  $T_{ij}$  within the flow can be included by choosing an integration surface that contains all of the volume with significant  $T_{ij}$  contributions.

The other terms on the right-hand-side of Eq. (1) include terms that are determined by the unsteady flow-field data on the integration surface. Provided that the unsteady flow data on the integration surface  $f = 0$  is correct, Reference 15 demonstrated that the FW-H equation correctly propagates the acoustic radiation from several source regions, including the complex signals associated with acoustic scattering from sharp edges.

The extremely small time step required in the RANS calculation to adequately resolve the high-frequency flow physics resulted in a limited temporal duration of the data. The total time represented by the unsteady calculation was 0.68 ms, approximately long enough for an acoustic wave generated at the leading edge of the main element to propagate halfway down the cruise-wing chord  $C$ . Because of the short time duration, the initial transient is important even when attention is restricted to the vicinity of the slat. Figure 4 shows the perturbation pressure signal at the slat trailing edge, the slat cusp, and the slat leading edge. To account for the rapidly decaying amplitude of the fluctuating pressure, relative to the scale of the pressure fluctuations at the slat trailing edge, the scale of the pressure fluctuations is magnified by a factor of 40 at the slat cusp and a factor of 200 at the slat leading edge. Although the data at the slat trailing edge is quasi-periodic from the start, over 0.2 ms pass before the transient goes by the slat cusp and almost 0.38 ms pass before the transient propagates past the slat leading edge. After passage of the initial transient,

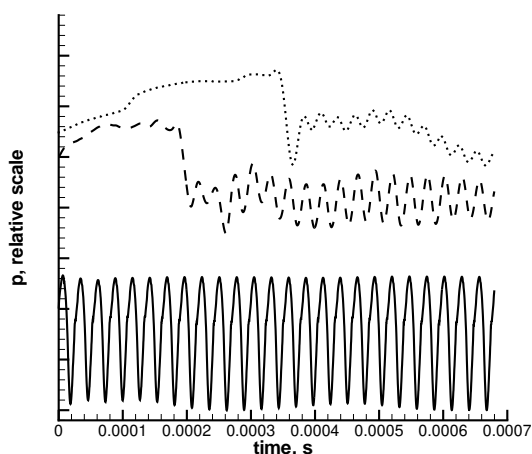


Figure 4. Perturbation pressure as function of time. Slat deflection is 30 degrees. — slat trailing edge, - - - - slat cusp, ····· slat leading edge. Vertical scale for data at slat cusp is magnified by factor of 40 and shifted. Vertical scale for data at slat leading edge is magnified by a factor of 200 and shifted.

a quasi-periodic condition prevails at all locations. To limit the effect of the transient, the first 25 percent of the data record is not used to produce the results presented here. Auxiliary calculations suggest that the use or nonuse of the first 25 percent of the data record produce relatively small quantitative variations in the results. All of the qualitative results are unchanged. To preclude any confusion, hereafter the term “data record” or any equivalents should be construed to refer to only the portion of the data that is actually used.

To deal with the limited data time series, a modified Hanning window is applied to the data. The modified Hanning window includes a standard Hanning filter for the first and last 12.5 percent of the data and a boxcar filter for the middle 75 percent. The windowed data is scaled to preserve the original energy in the signal. The resulting data sequence is then implicitly repeated as needed to provide an input signal of arbitrary duration. The windowing creates an artificial periodicity at approximately 1960 Hz, but because this frequency is much lower than the vortex shedding frequency, the artificial periodicity does not introduce any problems.

The application of acoustic theories to 2D flow data is a problem that is likely to become more visible as computational fluid dynamics (CFD) is relied upon more regularly to provide unsteady flow data

for use in acoustic calculations. Time-dependent, 3D, CFD data is extremely expensive to produce. In many applications, as in the current problem, the primary aerodynamic phenomena that generate noise are essentially 2D. The 3D effects are largely restricted to the fact that the true 3D unsteady flow structure is not completely correlated in the third direction. Cox et al.<sup>18</sup> computed 2D and 3D vortex shedding over circular cylinders and then used the results to calculate the acoustic pressure at an observer location. To use the 2D CFD computations, the acoustic calculations were performed by assuming perfect spanwise correlation of the flow over a finite span. They found that the acoustic amplitude could increase by as much as 20 dB simply by extending the finite span from 5 to 100 cylinder diameters.

As a first approximation, a 2D version of the FW-H equations is used to predict the sound field. Here we use the code developed by Lockard<sup>19</sup> for computing the 2D acoustic field from 2D CFD data. As noted above, we expect the 2D results to have greater amplitudes than those observed in the experiment, but the qualitative features of the acoustics are not expected to differ substantially. To study the effects of the spanwise correlation length, a limited number of 3D acoustic calculations are performed using the same FW-H code as was used in Ref. 15. As input to the 3D code, the 2D CFD data is repeated for a finite distance in the spanwise direction. Previous tests on idealized problems confirm that the 3D FW-H code and the 2D FW-H code give identical results for model problems when the spanwise extent is sufficiently long.

For consistency, all of the acoustic calculations are performed for observers located a fixed distance from the trailing edge of the slat. The fixed distance corresponds to the distance from the slat trailing edge to the centroid of the acoustic array. Directivity angles are indicated in Fig. 1; 0 degrees is in the downstream direction, 270 degrees is groundward in normal flight, towards the microphone array in the wind tunnel.

Another important issue involves the choice of integration surface for the FW-H calculation. Figure 5 illustrates the two integration surfaces that have been used for the FW-H calculations for the cases with a slat trailing-edge thickness  $h/C \approx 0.0007$ . The solid lines correspond to the component surfaces that lie on the solid bodies of the slat and main element. This combination of surfaces is designated the “on-body surface.” Because the limited time sample is insufficient for acoustic signals to propagate from the leading-edge slat to the trailing flap, the

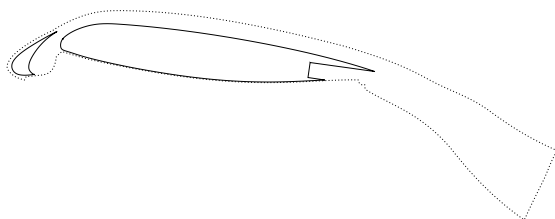


Figure 5. Integration surfaces used for FW-H calculations with  $h/C \approx 0.0007$ ; — on-body surface; ..... off-body surface.

information on the flap is not included. If it were included, it would contribute nothing to the noise because the computations show that the flow in the vicinity of the flap is steady. The dotted line corresponds to a permeable mathematical surface that contains within it the boundary layers on all three elements of the high-lift system as well as the region where the shed vortices reside. This integration surface includes all the major noise sources in this flow, and is designated the “off-body surface.” Because the flow-field quadrupole contributions to the noise are contained within the off-body surface, the neglected  $T_{ij}$  term in Eq. (1) is essentially zero for this case and little approximation is made by not integrating it explicitly. Although this consideration suggests that the off-body surface is a better choice than the on-body surface, in practice CFD grid resolution issues complicate the choice. Because of the limited order of accuracy of the CFD calculations,<sup>14</sup> flow fluctuations that are present on the on-body surface may have been numerically dissipated and dispersed by the CFD computation before the fluctuations arrive on the off-body surface, especially in the region between the pressure surface of the slat and the leading edge of the main element.

The deficiencies in the CFD grid between the slat and the main element have been minimized by refining the grid for the calculation with the slat trailing-edge thickness  $h/C \approx 0.0009$ . In addition, our experience with the prior calculations suggested that data be saved on a number of additional integration surfaces. Close-up views of these integration surfaces in the vicinity of the slat are shown in Figs. 6 and 7. For convenience, the four integration surfaces used for the  $h/C \approx 0.0009$  case are labeled 0–3. A brief description of each surface is given in Table 1. In Fig. 6 the solid lines (surface 0) represent the physical surfaces and correspond to the on-body integration surfaces used in the  $h/C \approx 0.0007$  cases. The dotted lines (surface 3) indicate a surface that includes all boundary layers and wakes and cor-

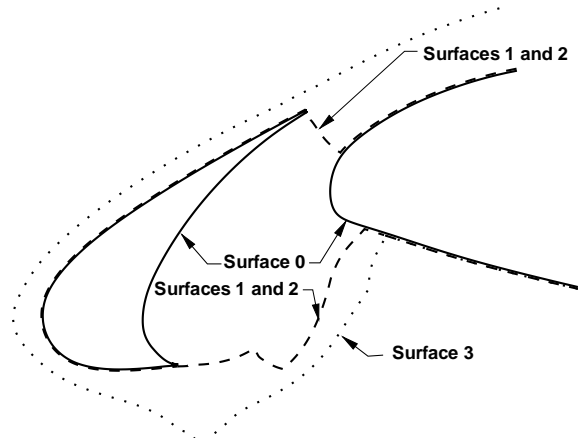


Figure 6. Integration surfaces used for FW-H calculations with  $h/C \approx 0.0009$ ; — on-body (surface 0); - - - - outside of boundary layers and cove (surfaces 1 and 2, see Fig. 7 to distinguish); ..... far outside of wakes and boundary layers (surface 3).

responds closely to the off-body integration surface used in the  $h/C \approx 0.0007$  cases. The dashed lines (surfaces 1 and 2) are intermediate surfaces that extend just outside of the boundary layers and include the entire cove region between the slat and main elements. The distinction between surface 1 and 2 is shown in Fig. 7. Surface 1 (shown with the dashed line) does not include the shed vortices in the wake of the slat while surface 2 (shown with the dotted line) includes a region that contains a limited number of the shed vortices. Surfaces 1 and 2 are believed to offer the most reasonable compromise between inclusion of acoustic sources and adequate CFD grid resolution from the sources to the integration surfaces.

## Results

Figure 8 shows computed spectra based on  $1/12^{\text{th}}$  octave bins for an observer located at 270 degrees. Only results for the on-body integration surfaces are shown. For the slat deflection of 20 degrees, the small-amplitude peak around 45 kHz is a residue of the initial transient. The analysis of the data in Ref. 14 shows no sustained vortex shedding in the CFD flow results for the 20 degree slat deflection. The corresponding FW-H spectrum essentially confirms the intuitively obvious result that no significant noise radiates. On the other hand, the vortex

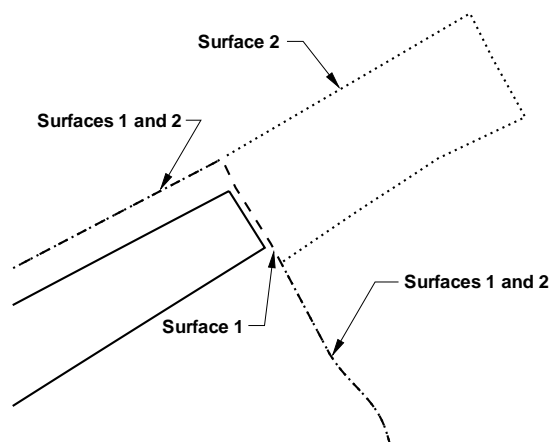


Figure 7. Close-up view of slat trailing edge; — surface 0; - - - - surface 1; ····· surface 2. Note that surface 1 and surface 2 share boundaries away from slat trailing edge.

Surface	Description
0	on body
1	off body – just outside boundary layers and cove
2	includes surface 1 and small region behind slat trailing edge
3	far outside of all wakes and boundary layers

Table 1. Description of integration surfaces.

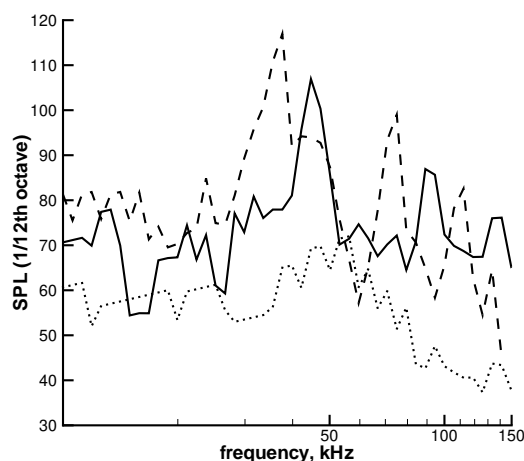


Figure 8. Spectra for observer positioned at 270 deg using on-body integration surfaces; — 30 deg slat deflection,  $h/C \approx 0.0007$ ; ····· 20 deg slat deflection,  $h/C \approx 0.0007$ ; - - - - 30 deg slat deflection,  $h = 0.0197$  in.

shedding associated with the 30 degree slat deflection produces intense noise, peaking around 45 kHz for the  $h/C \approx 0.0007$  case and at about 38 kHz for the  $h/C \approx 0.0009$  case. As expected, the thicker slat trailing edge results in stronger disturbances and louder noise levels. The lower frequency peak for the thicker trailing edge is consistent with the expectation of Strouhal scaling for the vortex shedding. However, the 27% increase in trailing-edge thickness results in an approximately 16% decrease in dominant frequency. Clearly, the trailing-edge thickness is not the only important flow parameter. Hammond and Redekopp<sup>20</sup> suggest the use of the body thickness plus the displacement thicknesses as the appropriate length scale for Strouhal scaling. Figure 9 shows the spectra for both trailing-edge thicknesses when comparable off-body integration surfaces are used. The dominant frequencies and general trends remain unchanged.

Although the frequency of maximum noise does not vary with differing integration surfaces, the directivity pattern is sensitive to the choice of integration surface. Figure 10 shows directivity patterns for the on- and off-body integration surfaces with  $h/C \approx 0.0007$ . In this figure, at any angle, the distance from the origin is proportional to the integrated pressure spectrum that radiates at the chosen angle. The solid line represents the directivity computed with CFD data on the on-body surface while the dashed line represents the directivity computed

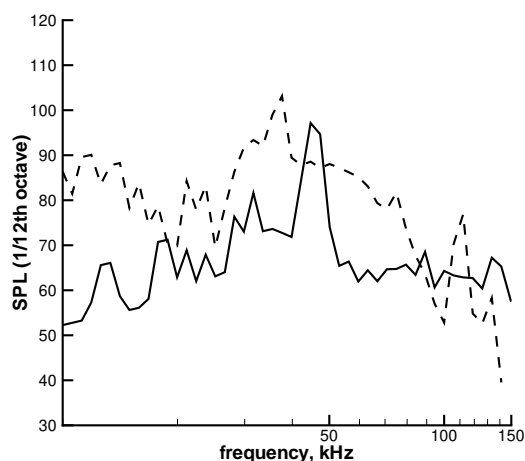


Figure 9. Spectra for observer positioned at 270 deg using off-body integration surfaces with 30 deg slat deflection; —  $h/C \approx 0.0007$ ; - - -  $h/C \approx 0.0009$ .

with the CFD data from the off-body surface. Significant qualitative differences exist, especially with regard to the strong upstream and downward directivity projections associated with the on-body integration surface. Without experimental directivity measurements or another calculation that better resolves the acoustic signals in the region between the on- and off-body integration surfaces, choosing which integration surface provides the more realistic prediction is difficult. Fortunately, the  $h/C \approx 0.0009$  calculation provides adequate grid resolution to a variety of off-body surfaces.

Figure 11 shows the directivity patterns that are obtained from the integration surfaces used with the thicker trailing-edge case. Many features of the directivity patterns are similar for both the  $h/C \approx 0.0007$  calculation and the  $h/C \approx 0.0009$  calculation. In particular, for the on-body integration surfaces, strong noise radiation is directed slightly above and below 180 degrees and at approximately 90, 225, and 270-300 degrees. These strong directivity projections exist for both slat trailing-edge thicknesses. As would be expected, the presence of the main element blocks significant acoustic radiation in the downstream direction. The use of off-body integration surfaces has a similar effect for both trailing-edge thickness cases. The strong upstream-directed projections slightly above and below 180 degrees, which are associated with the on-body integration surfaces, merge and have reduced levels. The acoustic radiation peak directed at approximately 225 de-

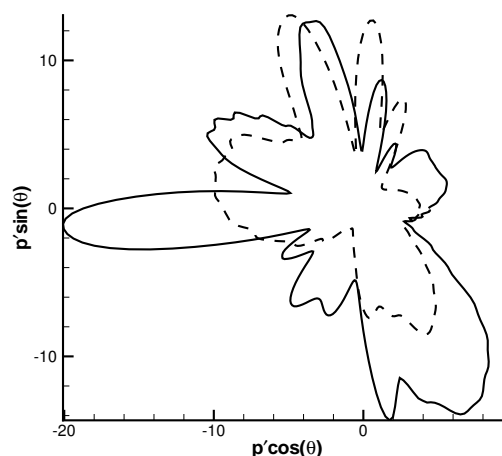


Figure 10. Directivity of acoustic signal for  $h/C \approx 0.0007$ ; — on-body surface; - - - off-body surface.

grees essentially disappears when off-body integration surfaces are used and the strong downwardly-directed acoustic radiation is reduced in amplitude.

The directivity patterns for off-body surfaces 1–3, shown in Fig. 11 are generally similar. However, where differences occur, simple explanations or trends are lacking. For instance, surface 3, which includes the entire slat wake, suggests stronger radiation in the 90–120 degree range than does either surface 1 or 2. However, the use of surface 2, which includes some of the slat wake, results in less acoustic radiation in this region than does the use of surface 1, which includes none of the slat wake. Therefore, no clear trend exists with respect to the inclusion of additional portions of the slat wake. Similarly, no clear trend exists in the 330–360 degree range. In this angular range, the noise radiated from surface 3 is less than that radiated from either surface 1 or surface 2, but the noise radiated from surface 2 is slightly greater than that radiated from surface 1.

Although the acoustic array used in the experiment was not intended to provide any directivity information, the high-frequency acoustic signal was so loud that it overwhelmed the intrinsic wind-tunnel noise and can be identified from the spectrum of some of the individual microphones used in the acoustic array. The relative amplitudes of the mean square fluctuating pressure in a frequency range around 50 kHz from a subset of microphones having approximately the same cross-stream location are shown in Fig. 12. The abscissa in the figure indicates streamwise distance. The microphone lo-



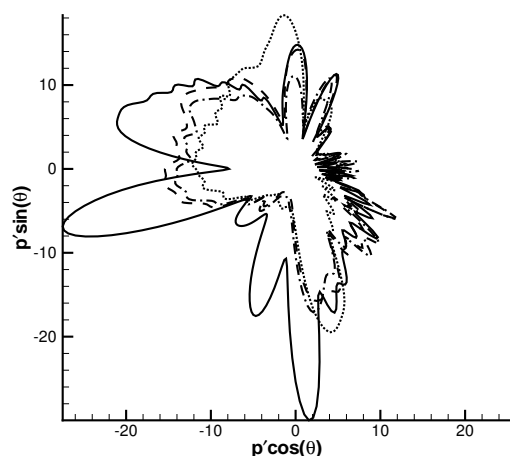


Figure 11. Directivity of acoustic signal for  $h/C \approx 0.0009$ ; — on-body surface (surface 0); - - - surface 1; - · - · - surface 2; · · · · surface 3.

cations are shown as squares in the figure and their positions relative to the airfoil are easily deduced. The computed mean square fluctuating pressure projected to the acoustic-array surface is shown as the dashed line. The computed results are calculated using integration surface 1. The maximum amplitude of the microphone data is scaled with the maximum amplitude of the calculation. Far upstream of the airfoil, both the microphone response and the computed noise level are flat. The non-zero microphone response is probably associated with the wall-pressure fluctuations of the turbulent boundary layer along the wind-tunnel ceiling. These fluctuations are not included as part of the CFD calculations. Slightly upstream of the slat leading edge, the noise level rises. Unfortunately the construction of the wind tunnel prevented the positioning of microphones over an extensive region that would include the streamwise location of the slat trailing edge. The maximum amplitude occurs in the mid-chord region followed by a sharp drop in amplitude. The qualitative features of the computations agree remarkably well with the microphone data and have been used to aid in the redesign of the acoustic array for a future wind-tunnel test.

In the actual flow, the vortex-shedding process is not perfectly correlated in the spanwise direction. The correlation between two points is reduced as the spanwise distance between them increases. The physical decorrelation process could be modeled as a random walk, however numerical integration over a

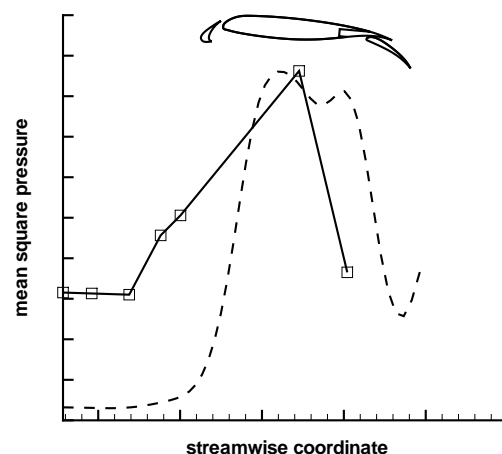


Figure 12. Comparison of squared acoustic pressure at individual microphones to that predicted computationally for  $h/C \approx 0.0009$  case using integration surface 1. Microphone positions and values are shown with squares; dashed line indicates computationally predicted values.

very large distance in the spanwise direction would then be required. Here we model the effects of the span by assuming perfect correlation along a fixed spanwise distance with no contribution from points outside of this distance. The half-span used in the calculations is denoted by  $L_z$  and it is normalized with the cruise-wing chord  $C$ . The observers are positioned a distance  $d = 2C$  from the slat trailing edge.

To estimate the sort of behavior that we might expect for the 3D acoustic calculation, we first examine the analytically predicted behavior of a continuous line source in the spanwise direction. For this source, the contribution to the pressure will vary in the spanwise direction as

$$\frac{1}{\sqrt{1 + (z/d)^2}} \exp(i\omega d/c \sqrt{1 + (z/d)^2}) \quad (4)$$

where  $z$  is the spanwise coordinate and the observer is located at  $z = 0$ . The leading factor  $1/\sqrt{1 + (z/d)^2}$  controls the decay of the amplitude of the acoustic contribution as the source points move away from the observer. The terms in the exponential determine the spatial periodicity. For small  $z$ , the spanwise oscillation period is large, but the period decreases with increasing  $z$ . To reduce the spanwise oscillation amplitude to 10 percent of its  $z = 0$  value requires that  $z \approx 10d$ , or, for the cases studied here, about 11 meters. This distance

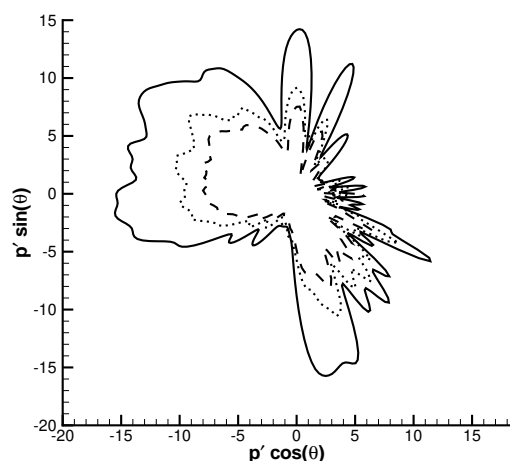


Figure 13. Directivity of acoustic signals for  $h/C \approx 0.0009$ ;  $---$   $L_z/C = 0.25$ ;  $\cdots$   $L_z/C = 2.0$ ;  $—$  2D calculation.

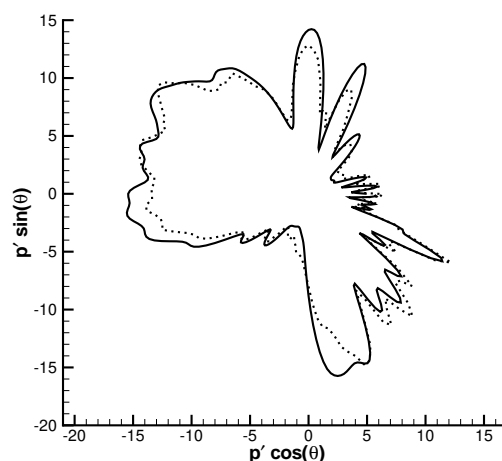


Figure 14. Directivity of acoustic signals for  $h/C \approx 0.0009$ ;  $\cdots$   $L_z/C = 2.0$  scaled by a factor of 1.4;  $---$  2D calculation.

is far greater than the wind-tunnel span, and would clearly be much greater than any reasonable estimate of the spanwise coherence. These estimates suggest that the 2D calculations are likely to substantially overpredict the amplitude of the acoustic field. Further analysis of Eq. (4) suggests that near  $z = 0$ , the spanwise oscillation period  $z_p$  for a 38 kHz source is  $z_p/C \approx 0.26$ , but that for large  $z$ , the oscillation period is much smaller, with  $z_p/C \approx 0.015$ . The variation of the oscillation period requires that spanwise grid-resolution requirements be reviewed whenever the spanwise extent changes.

Because 3D acoustic calculations are much more expensive than their 2D counterparts, 36 observers (spaced ten degrees apart) are used in an initial set of 3D acoustic calculations to determine trends with variation of the spanwise extent  $L_z$ . Only data on integration surface 1 was used for these calculations. After ascertaining the spanwise resolution requirements and finding no unexpected tendencies, acoustic calculations using  $L_z/C = 0.25$  and  $L_z/C = 2.0$  were performed with 180 observers spaced two degrees apart. The directivity patterns are compared with the results from the 2D calculation in Fig. 13.

Examination of Fig. 13 reveals some interesting trends. As expected, with increased spanwise extent the noise increases. Cases run with  $0.25 < L_z/C < 2.0$  show that the increase in noise is not monotonic, varying instead with the spanwise period. Cox et al.<sup>18</sup> observed a similar trend until, at some value of  $L_z$ , the average noise level asymptoted and only small variations associated with the periodicity in  $z$

were observed. Our data suggest that the qualitative features of even a complex directivity pattern establish themselves at relatively small values of  $L_z$ . In Fig. 13 all of the directivity lobes found in the 2D results can be traced back to corresponding lobes obtained with both  $L_z/C = 2.0$  and  $L_z/C = 0.25$ . Recall that  $L_z/C \approx 0.26$  corresponds to the spanwise period in Eq. (4) for  $z \approx 0$ ; therefore the basic directivity features are established within the first spanwise period.

Although uniform scaling of the small-to-moderate  $L_z$  results does not exactly replicate the 2D directivity pattern, such a simple scaling is a reasonable estimate. A comparison of the 2D results and the  $L_z/C = 2.0$  results scaled by a factor of 1.4 is shown in Fig. 14. The agreement between the two is surprisingly good. However, the scaling factor was determined empirically. Efforts to derive the scaling factor have been unsuccessful thus far. For instance, the ratio obtained by dividing the amplitude of the integration of Eq. (4) from  $z = -\infty$  to  $z = \infty$  by the amplitude of the the integration from  $z = -L_z$  to  $z = L_z$  might be expected to approximate the scaling factor. However, this ratio is in the range of 1.03, rather than the observed 1.4. Variations on this theme, such as taking ratios of only the real or imaginary parts produced similarly disappointing results. Additional work still needs to be done to take full advantage of the 2D acoustic solution in this type of quasi-2D flow.

### Conclusions

Data from highly resolved, unsteady, 2D RANS calculations of a high-lift configuration with a blunted slat trailing edge were used to perform acoustic analyses using the permeable-surface FW-H equation. The results lend support to the hypothesis proposed by Khorrami et al<sup>14</sup> that vortex shedding from the trailing edge of the slat is responsible for a loud, high-frequency noise observed in a corresponding set of experiments. A 2D FW-H solver<sup>19</sup> was used to evaluate the noise using a variety of different integration surfaces. The use of an on-body integration surface produced suspiciously large directivity lobes directly upstream and towards the microphone array. The use of off-body integration surfaces that include the slat-cove region modified the directivity pattern considerably. Alternative off-body integration surfaces that include the slat-cove region produced similar results. Comparison of mean-square pressure results with data from individual microphones in the acoustic array showed qualitatively similar trends.

A number of 3D acoustic calculations were performed by replicating the 2D RANS data in the spanwise direction for varying spanwise extents. As expected, the noise generally increased with increasing spanwise extent. All of the important directivity lobes observed in the 2D acoustic results were observed at the smallest spanwise extent tested. A simple scaling of the 3D directivity pattern compared favorably with the 2D directivity pattern. Unfortunately, to date, the scaling factor can only be obtained empirically, after both the 2D and 3D cases have been computed. A method for modeling the scaling factor would greatly enhance the predictive usefulness of the 2D solution.

### Acknowledgments

The authors thank Dr. Craig Streett, Dr. Robert Stoker, Jim Underbrink, and Guy Neubert for the use and analysis of the experimental data.

### References

1. Davy, R. and Remy, H., "Airframe Noise Characteristics on a 1/11 Scale Airbus Model," AIAA Paper No. 98-2335, June 1998.
2. Hayes, J. A., Horne, W. C., Soderman, P. T., and Bent, P. H., "Airframe Noise Characteristics of a 4.7% Scale DC-10 Model," AIAA Paper No. 97-1594, 1997.
3. Dobrzynski, W., Nagakura, K., Gehlhar, B., and Buschbaum, A., "Airframe Noise Studies on Wings with Deployed High-Lift Devices," AIAA Paper No. 98-2337, June 1998.
4. Macaraeg, M. G., "Fundamental Investigations of Airframe Noise," AIAA Paper No. 98-2224, June 1998.
5. Meadows, K. R., Brooks, T. F., Humphreys, W. M., Hunter, W. H., and Gerhold, C. H., "Aeroacoustic Measurements of a Wing-Flap Configuration," AIAA Paper No. 97-1595, May 1997.
6. Khorrami, M. R., Singer, B. A., and Takallu, M. A., "Analysis of Flap Side-Edge Flow Field for Identification and Modeling of Possible Noise Sources," SAE Paper No. 971917, May 1997.
7. Takallu, M. A., and Laffin, K. R., "Reynolds-Averaged Navier-Stokes Simulations of Two Partial-Span Flap Wing Experiments," AIAA Paper No. 98-0701, January 1998.
8. Streett, C. L., "Numerical Simulation of Fluctuations Leading to Noise in a Flap-Edge Flowfield," AIAA Paper No. 98-0628, January 1998.
9. Streett, C. L., "Numerical Simulations of a Flap-Edge Flowfield," AIAA Paper No. 98-2226, June 1998.
10. Khorrami, M. R., Singer, B. A., and Radeztsky, R. H., J., "Reynolds-Averaged Navier-Stokes Computations of Flap-Side-Edge Flowfield," *AIAA J.*, Vol. 37, No. 1, January 1999, pp. 14-22.
11. Khorrami, M. R., and Singer, B. A., "Stability Analysis for Noise-Source Modeling of a Part-Span Flap," AIAA Paper No. 98-2225, June 1998.
12. Morgan, H. L., "Model Geometry Description and Pressure Distribution Data from Tests of EET High-Lift Research Model Equipped with Full-Span Slat and Part-Span Flaps," NASA TM 80048, 1979.
13. Underbrink, J. R., and Dougherty, R. P., "Array Design for Non-intrusive Measurements of Noise Sources," Noisecon 96, 1996.
14. Khorrami, M. R., Berkman, M. E., Choudhari, M., Singer, B. A., Lockard, D. L., and Brentner, K. S., "Unsteady Flow Computations of a Slat with a Blunt Trailing Edge," AIAA Paper No. 99-1805, May 1999.

15. Singer, B. A., Brentner, , S., K., Lockard, D. L., and Lilley, G. M., "Simulation of Acoustic Scattering from a Trailing Edge," AIAA Paper No. 99-0231, January 1999.
16. Ffowcs Williams, J. E., and Hawkings, D. L., "Sound Generated by Turbulence and Surfaces in Arbitrary Motion," *Philosophical Transactions of the Royal Society*, Vol. A264, No. 1151, 1969, pp. 321-342.
17. Brentner, K. S., and Farassat, F., "An Analytical Comparison of the Acoustic Analogy and Kirchhoff Formulation for Moving Surfaces," *AIAA Journal*, Vol. 36, No. 8, 1998, pp. 1379-1386.
18. Cox, J. S., Brentner, K. S., and Rumsey, C. L., "Computation of Vortex Shedding and Radiated Sound for a Circular Cylinder: Subcritical to Transcritical Reynolds Numbers," *Theoretical and Computational Fluid Dynamics*, Vol. 12, No. 4, 1998, pp. 233-253.
19. Lockard, D. P., "An Efficient, Two-Dimensional Implementation of the Ffowcs Williams and Hawkings Equation," submitted to *Journal of Sound and Vibration*, Jan 1999.
20. Hammond, D. A., and Redekopp, L. G., "Global Dynamics of Symmetric and Asymmetric Wakes," *Journal of Fluid Mechanics*, Vol. 331, 1997, pp. 231-260.